Polarization-modulation Approaches to Reflection–Absorption Spectroscopy

Brian L. Frey[1], Robert M. Corn[2] and Stephen C. Weibel[3]

[1] *Lake Forest College, Lake Forest, IL, USA*
[2] *University of Wisconsin – Madison, Madison, WI, USA*
[3] *GWC Instruments, Madison, WI, USA*

1 INTRODUCTION TO POLARIZATION-MODULATION REFLECTION–ABSORPTION SPECTROSCOPY

Infrared reflection absorption spectroscopy (IRRAS) is a sensitive technique for characterizing the chemical structure and molecular orientation of thin films and monolayers adsorbed onto metal surfaces (see **Reflection–Absorption Spectroscopy of Thin Films on Metallic Substrates**). IRRAS measurements with Fourier transform infrared (FT-IR) spectrometers have become an established sampling method for films of thickness less than 200 nm.[1] FT-IR measurements of 1000 scans or more will produce monolayer spectra of reasonable signal-to-noise ratio (S/N). However, the sensitivity of these measurements is often limited because the thin sample layer has several orders of magnitude fewer molecules than in a conventional infrared transmission experiment,[2] and the bands of interest from surface species are often obscured due to atmospheric background absorption, which can change over the time of the measurement. In addition, this reflection technique involves the measurement of very small absorptions on a large background signal. As a result the dynamic range of the FT-IR spectrometer signal channel can impose limitations on the minimum detectable absorbance.[1] Another practical concern is that instrument drift and alignment sensitivity at grazing-angle incidence make it difficult to measure a background reference that will produce a final sample spectrum free of baseline artifacts. In situ measurements of surface species, especially at the interface of a metal surface and a solution, are very challenging.

By taking advantage of the polarization selectivity of the surface absorption,[3] these difficulties in metal surface reflection measurements can be overcome. At a high (grazing) angle of incidence, the absorption of p-polarized infrared radiation by a thin film on a metal surface is enhanced so that even submonolayer quantities of chemisorbed species can be observed in the p-polarized infrared reflectance spectrum. In contrast, at a high angle of incidence, the absorption of s-polarized radiation by the same film is virtually zero. This polarization disparity leads to strong selection rules at the surface, and has been used to deduce the average molecular orientation and conformation for monolayers of molecules adsorbed onto metals.[4–6] In addition to orientation measurements, the greatly increased absorption of p-polarized over s-polarized radiation by thin films at the metal surface can be utilized to obtain the differential reflectance spectrum of the adsorbed surface species by polarization modulation (PM) of the infrared light. The combination of PM, FT-IR spectrometry and reflection measurements at grazing incidence yields a sensitive and surface-selective method for obtaining infrared reflection–absorption spectra of very thin films on metal substrates.

2 EXPERIMENTAL CONSIDERATIONS FOR THE PM-IRRAS MEASUREMENT

2.1 Experimental setup

Because of component physical sizes and optical requirements it is not practical to set up the PM-IRRAS experiment

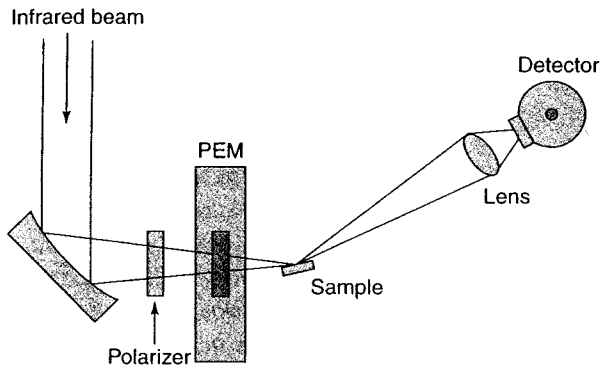

Figure 1. PM-IRRAS optical layout.

in most FT-IR spectrometer sample compartments. The optical layout for the grazing-angle reflection measurement using the external beam port from an FT-IR spectrometer is depicted in Figure 1. A collimated infrared light beam from the external port of the spectrometer is directed to an off-axis parabolic mirror with a long focal length. The light is focused onto the sample surface at an effective incident angle of 75° to 80°. Prior to the sample, the light beam passes through a wire grid polarizer and a photo-elastic modulator (PEM). After the sample, the beam is collected with an infrared lens and focused onto the detector element.

If the collimated beam diameter is 3.6 cm, a parabolic mirror with an effective focal length (EFL) of 15 cm would result in a convergent beam with a half-angle of 7°. This geometry restricts the median grazing incident angle to an angle of less than 83° to avoid the extreme ray missing the sample surface.[1] An off-axis parabolic mirror with an EFL of 25 cm results in a half-angle of 4° for the same collimated beam diameter, and is often the size required when directing the beam onto a sample in an ultrahigh vacuum (UHV) chamber.

The polarizer for the mid-infrared spectral region is fabricated with a grid of closely spaced parallel metal wires etched onto an infrared transmitting substrate (usually BaF_2 or ZnSe). These grid polarizers are produced at the National Physical Laboratory in the UK and have a wire grid spacing of 250 nm. They are sold by Specac (Orpington, UK). The transmission axis of the grid polarizer is actually perpendicular to the direction of the grid orientation. The polarizer is mounted so the transmission axis is at an angle of 45° to the optical axis of the PEM.

The PEM (manufactured by Hinds Instruments, Hillsboro, OR, USA) is an optical device that modulates the polarization state of the input light beam at a fixed frequency (usually 37 kHz or 50 kHz depending on model). It operates by inducing birefringence in an isotropic optical element (typically ZnSe in the mid-infrared region) at a resonant frequency related to the size and shape of the element. Because the modulation efficiency varies across the element radius the infrared beam should be centered in the PEM element aperture.

The sample mount design is an often-overlooked part of the IRRAS experiment. Typical sample metal films are roughly 1 cm in diameter and must be mounted with reproducible positioning to minimize background baseline variations. The sample mount must also not allow reflected stray light to reach the detector. Since the beam size in the plane of the reflection at the sample surface varies inversely with the cosine of the incident angle,[1] the infrared beam image at the sample surface is elongated. This elliptical beam shape can result in light being reflected off the edges of the sample mount and reaching the detector to produce spectral artifacts. A "notch" in the sample mount on both sides of the sample film will prevent stray light from being imaged to the detector.

Any polarization-sensitive optical components between the sample surface and detector can produce a polarization difference signal resulting in a source of spectral artifacts. Because the light reflected from a parabolic mirror has a polarization dependence, a single lens after the sample is used to collect the reflected light and focus it onto the detector.[7] Infrared lenses (BaF_2 or ZnSe) with focal ratios of $f/1$ or $f/1.5$ are available from Janos Technology (Townshend, VT, USA). Lens mounting with excessive compression can induce birefringence in the lens causing artifacts. The detector vacuum Dewar window and detector element are also potential sources of birefringence.

The optimum detector for measurements throughout the mid-infrared is a narrow-band mercury cadmium telluride (MCT) type detector ($D^* = 5 \times 10^{10}\,\mathrm{cm\,Hz^{1/2}\,W^{-1}}$) with an element area of 1 mm^2. An InSb detector will provide increased sensitivity but only responds to wavenumbers greater than 1800 cm^{-1}. The high throughput of the PM-IRRAS experiment does lead to nonlinearity in the MCT detector, and therefore requires detector linearization procedures to obtain spectra with nice baselines. The details of this procedure depend greatly upon the particular MCT since each company attaches its own pre-amplifier circuit with various trimpots affecting the linearity. The company should provide assistance in adjusting the linearity of the MCT detector, but in the end it is essentially an empirical optimization achieved by looking at the resulting spectra.

2.2 The PEM

The photoelastic effect is the basis for the operation of a PEM to manipulate light polarization.[8] A piezoelectric transducer attached to a ZnSe crystal alternately compresses or stretches a ZnSe element at a resonant frequency (37 kHz or 50 kHz). The resonance is induced by applying a driving voltage to the piezoelectric transducer, and

this resonant design restricts the PEM to a fixed frequency. The stressed ZnSe element becomes birefringent with the index of refraction varying with the driving frequency and has maximum birefringence at the center of the element. This refractive index variation is wavelength dependent and its maximum variation is a function of the driving voltage amplitude. The PEM functions as an optical waveplate on an input-polarized light beam.

If the plane of polarization of the input light is at an angle of 45° to the modulator optical axis, then, at a particular light wavelength, the PEM acts as a half-wave plate at the time of maximum compression or stretching of the ZnSe element. The output light plane of polarization is then orthogonally rotated at this moment in the cycle. Since the output polarization state is 180° apart at the peak compression and stretching time, the actual linear PM is twice the resonant frequency (100 kHz for a 50 kHz resonant modulator). In other words, the PEM is a half-wave plate (at a particular wavelength) twice during each PEM cycle. The wavelength at which the PEM acts as a half-wave plate is referred to as the *half-wave retardation*. This retardation wavelength is dependent on the driving voltage amplitude and is controlled by the PEM control electronics. Between successive linear polarization states the light is elliptically polarized and is circularly polarized at the particular moment when the PEM is at the *quarter-wave retardation* point in the cycle. The PM superimposes a high-frequency signal on the normal interferogram Fourier frequencies. The measured waveform of a portion of the modulated interferogram is shown in Figure 2. The intensity of the high frequency modulation is the difference PM-IRRAS signal.

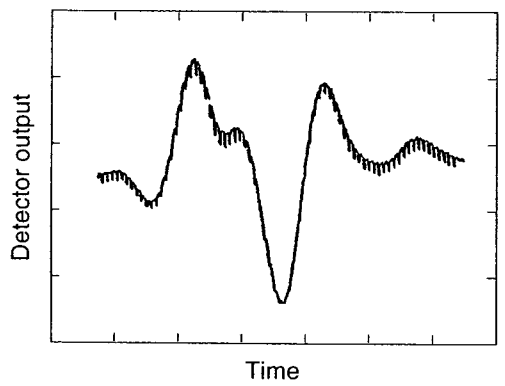

Figure 2. Measured PM-IRRAS interferogram signal obtained prior to demodulation. The high-frequency signal is from the PM. The intensity of the high-frequency modulation is the differential PM-IRRAS signal and must be demodulated in the presence of the relatively large variation in the average interferogram signal. (Reproduced from Barner *et al.*[9] with permission from the American Chemical Society.)

2.3 The PM-IRRAS measurement

The first PM-IRRAS measurements were made following the development of PM-FT-IR vibrational circular dichroism (VCD) techniques.[2] Similar to the VCD technique, the polarization-modulated signal of 74 kHz was demodulated with a lock-in amplifier, and the optical velocity was $0.3\,cm\,s^{-1}$. A film of cellulose acetate on copper was measured with the conventional IRRAS method and with PM-IRRAS; both spectra are shown in Figure 3. These measurements showed a somewhat improved S/N because of the dynamic range reduction in the PM-IRRAS experiment. Even more dramatic, however, was the demonstration that PM-IRRAS is sensitive only to molecules on the surface and rejects background water vapor absorption ($1350-1850\,cm^{-1}$ region in Figure 3).

These improved PM-IRRAS measurements were restricted by some experimental limitations in the demodulation technique.[9,10] In order to ensure that the variations in the polarization difference signal did not exceed the

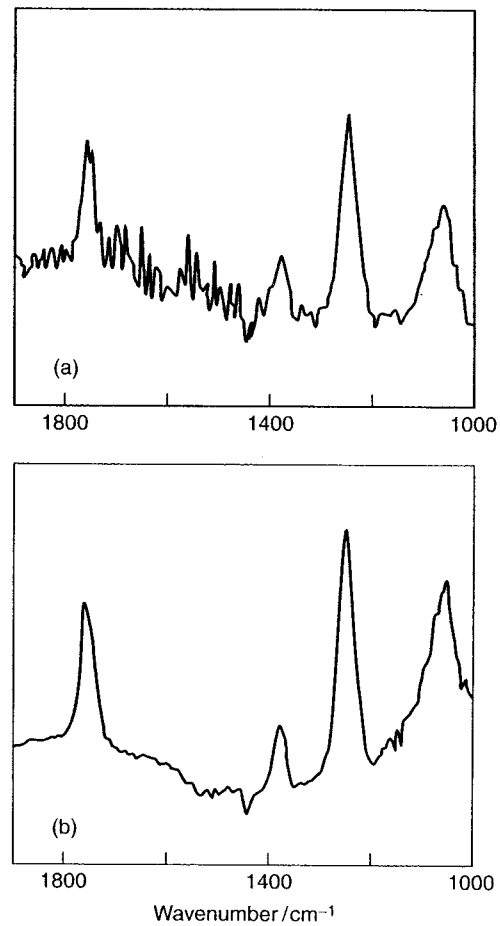

Figure 3. IRRAS spectra of the same 1-nm thick film of cellulose acetate on a copper surface taken (a) without and (b) with PM. (Reproduced from Dowrey and Marcott[2] with permission from the Society of Applied Spectroscopy.)

time constant of the lock-in amplifier output electronics, the interferometer mirror velocity was slowed down, diminishing the signal averaging capabilities of the instrument. The time constant of the lock-in amplifier is typically on the order of 0.5 ms, which requires the mirror velocity of the interferometer to be reduced so that the modulation frequencies in the interferogram fall below 2 kHz. Most FT-IR spectrometers are designed to operate at mirror velocities up to 20 times higher than this cut-off value. Spectrometers with variable mirror velocities are capable of running at velocities sufficiently low for this experiment; however, the measurement time is greatly increased. For instance, a measurement of 1000 scans in 10 min at a normal mirror velocity for an MCT detector becomes a measurement of more than 1 h with the lock-in amplifier.

To avoid these problems, a new demodulation technique was developed to measure the intensity I_p of the p-polarized light component minus the intensity I_s of the s-polarized component at the peak of the modulation cycle.[9,11] This direct measurement of the polarization difference signal permits the interferometer mirror to be scanned at higher velocities (0.5–1.5 cm s^{-1}). As depicted in Figure 4, the p-polarized component I_p is measured simultaneously to the extrapolated s-polarized component "I_s". This value of "I_s" can be estimated by a quadratic approximation method with sampled measurements at −180°, 0°, and 180° during each modulation cycle. The value of I_p is measured directly at the cycle peak $I_p(90)$, and the value of "I_s"(90) is estimated from the three points "I_s"(−180), "I_s"(0), and "I_s"(180) after synchronizing the sampling with the PEM controller phase. This synchronous sampling method generates a sum and a difference interferogram representing the signals $(I_p + I_s)$ and $(I_p - I_s)$, respectively. The Synchronous Sampling Demodulator (SSD) is produced by GWC Instruments (Madison, WI, USA). These interferograms are digitized in alternating blocks of mirror scans with the analog-to-digital converter (ADC) of the FT-IR spectrometer and Fourier-transformed to yield the sum and difference single-beam spectra, respectively. When ratioed to yield the differential reflectance spectrum, the baseline has a wavelength dependence which has the form of a second-order Bessel function because of the modulation efficiency of the PEM.[9,12]

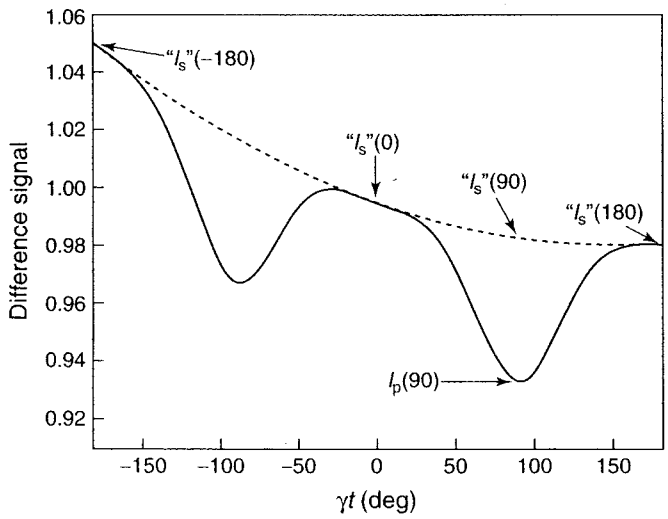

Figure 4. An expanded view of the interferogram shown in Figure 2 to show the methodology for sampling the real-time modulation signals I_p and "I_s" during the interferometer scan. The value of I_p is measured directly at 90° and the value of "I_s"(90) is estimated from the three measured points "I_s"(−180), "I_s"(0), and "I_s"(180). (Reproduced from Barner *et al.*[9] with permission from the American Chemical Society.)

2.4 PM-IRRAS spectral normalization

Figure 5 shows the spectrum of a monolayer of methyl *N*-(4-mercaptophenyl) carbamate on a gold substrate using the synchronous sampling method. The spectrum is the result of ratioing the difference single-beam spectrum to the sum single-beam spectrum and shows the sample absorption peaks on top of the wavelength-dependent efficiency curve of the PEM. Although the spectrum is in transmission units, the direction of the absorption peaks is upward because the measured signal is a polarization difference signal.

An expanded view of the spectrum is shown in Figure 6. The slowly varying background baseline can be fit with a polynomial function. It should be noted that the baseline correction must be done by dividing the spectrum by the polynomial function rather than by a subtraction because the sample spectrum baseline is an efficiency curve and varies with the PEM retardation control voltage.[13] A subtraction would reduce the relative peak intensities the farther the peak is from the efficiency curve maximum value.

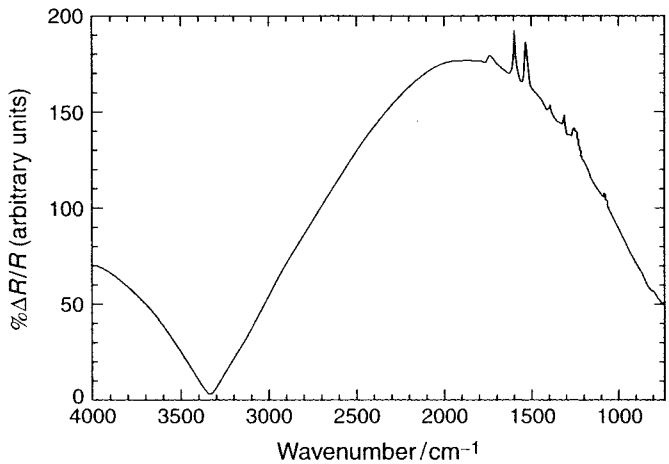

Figure 5. PM-IRRAS differential reflectance spectrum produced by ratioing the difference single beam to the sum single beam.

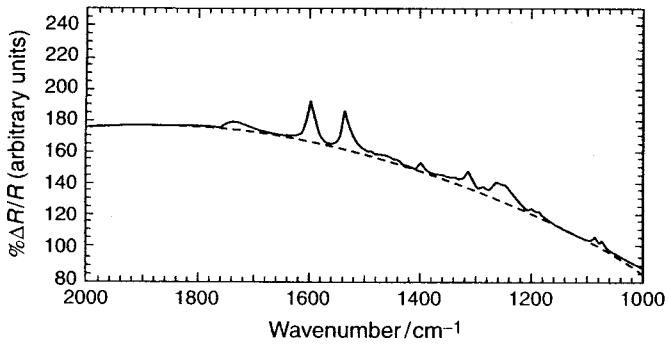

Figure 6. Expanded view of the PM-IRRAS spectrum with an overlay (dashed curve) of the baseline generated by curvefitting.

The baseline-corrected PM-IRRAS spectrum will give the correct relative peak intensities, but the question of how to determine the absolute spectral intensity remains. One way to calibrate the spectrum in order to find the absolute intensity is to repeat the measurement without the PEM but with the polarizer (with p-polarized light) and to use a clean metal substrate when acquiring the background. This spectrum would provide the correct intensities to calibrate the PM-IRRAS spectrum.

If the relative gain of the difference and sum channels of the demodulator is known, an improved method for determining the actual spectral intensity is possible. Equation (1) summarizes the procedure for normalizing the raw PM-IRRAS spectrum to the correct absolute spectral intensity:

$$\text{Spectrum } (\%T) = \left\{\left[-\left(\left\{\frac{[(\text{File}/100)/\text{Gain}]}{\text{Ref}}\right\} - Y_{\max}\right)\right] + 1\right\} \times 100 \quad (1)$$

where File is the measured difference divided by the sum of the percentage transmittance spectrum, Gain is the gain of the demodulator difference channel divided by the gain of the sum channel, Ref is a polynomial function fit to the measured spectrum baseline and scaled to a maximum intensity of 1, and Y_{max} is the peak baseline intensity value of the measured raw PM-IRRAS spectrum.

The only required information is the relative gain of the difference and sum signal channels. Other signal gains in the measurement will affect both channels equally. The maximum of the efficiency curve of the raw uncorrected PM-IRRAS spectrum is arbitrarily assigned to 100% reflectivity. This is the justification for subtracting the Y_{max} value and adding +1 to obtain the absolute intensity-corrected spectrum. Dividing by the actual gain value and by the normalized polynomial function is the part of the procedure which determines the correct intensities. Figure 7 is the normalized data showing the correct intensities of the monolayer spectrum of Figures 5 and 6. This normalization

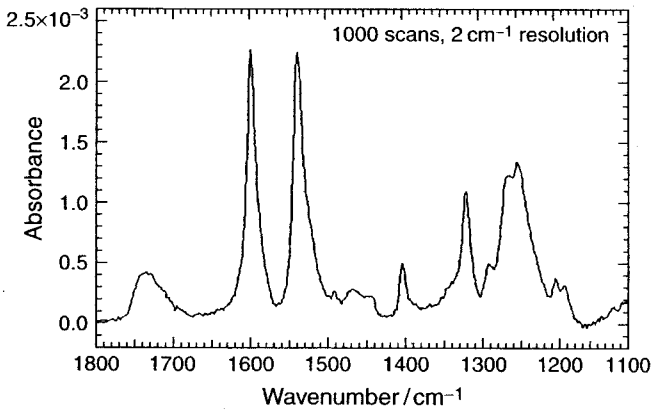

Figure 7. The baseline-corrected and intensity-normalized PM-IRRAS spectrum.

method permits the determination of the absolute spectral intensities of PM-IRRAS measurements without having to measure a metal reference surface.

3 EXAMPLES AND APPLICATIONS OF PM-IRRAS MEASUREMENT

The majority of work using PM-IRRAS has involved monolayers and thin films on reflective metal substrates, although the air/water interface has been studied as well. The first set of applications given in this section deals with ex situ measurements on metal surfaces. We have picked two examples from this area in order to demonstrate the types of information attainable, a few experimental details, and the advantages of the PM approach. The following two sections deal with measurements of a metal surface in contact with either a liquid or gaseous bulk phase. In situ measurements take fuller advantage of PM-IRRAS's capabilities, but the added difficulties with any in situ analysis have limited the number of examples in the literature. The final example demonstrates the ability of PM-IRRAS to detect the very small signals associated with monolayers at the air/water interface.

3.1 Metal surfaces – ex situ

3.1.1 Self-assembled monolayers in the CH stretching region

PM-IRRAS has been used most frequently for characterizing self-assembled monolayers (SAMs) primarily on gold surfaces. The most common SAMs are those formed from alkanethiol molecules containing a thiol functional group (–SH), usually a long alkyl chain of 10–20 methylene groups, and a terminal functional group such as methyl, hydroxyl, or a carboxylic acid. These SAMs utilize a strong

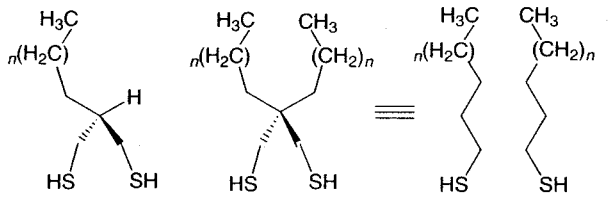

n = 10 (C14)	1	4	7
n = 12 (C16)	2	5	8
n = 13 (C17)	3	6	9
	m	d	n

Figure 8. Structures of the spiroalkanedithiols and normal alkanethiols used for generating SAMs on gold. (Reproduced from Shon *et al.*[14] with permission from the American Chemical Society.)

gold–sulfur interaction and a well-ordered packing of the alkyl chains to produce a stable, complete, single layer of molecules on the gold surface, namely a SAM. Lee and co-workers have studied the order and orientation of several new types of SAMs similar to the alkanethiols.[14] They found that subtle changes in molecular structure greatly affect the organization of the SAMs. For example, monolayers were prepared from the three classes of compounds shown in Figure 8: m, the monoalkyl spiro compound; d, the dialkyl spiro compound; and n, the normal alkanethiol. Three chain lengths were synthesized for each class, but let us consider only the C16 analogs. The differences in structure of these compounds lead to differences in packing order as evidenced by PM-IRRAS spectra in Figure 9. All spectra show four prominent peaks, which are assigned in the figure to the symmetric (ν_s) and asymmetric (ν_a) stretching vibrations of the CH_2 and CH_3 groups. Taking first the spectrum of the normal alkanethiol n-C16, the ν_a CH_2 band occurs at 2918 cm^{-1}, which has been shown to indicate well-ordered packing of the alkyl chains in a nearly all trans configuration with very few gauche defects. An increase in frequency of this band up to about 2930 cm^{-1}, however, indicates that the packing order has diminished to a more random liquid-like nature. The d-C16 spectrum shows this band at 2921 cm^{-1}, which indicates the monolayer is still reasonably well ordered. Finally, the monoalkyl compound m-C16 yields a peak position of 2925 cm^{-1}, which suggests it forms a significantly less ordered monolayer than the other types of molecules. Furthermore, the broadness of CH_2 bands and the larger intensity for the m-C16 monolayer provide evidence of diminished order and possibly even a greater tilt angle than the other monolayers.

Since the band position of the ν_a CH_2 band is indicative of the order in the monolayer, it has also been used to study the self-assembly process of monolayers.[15] An example is given in Figure 10, which shows the band position as a

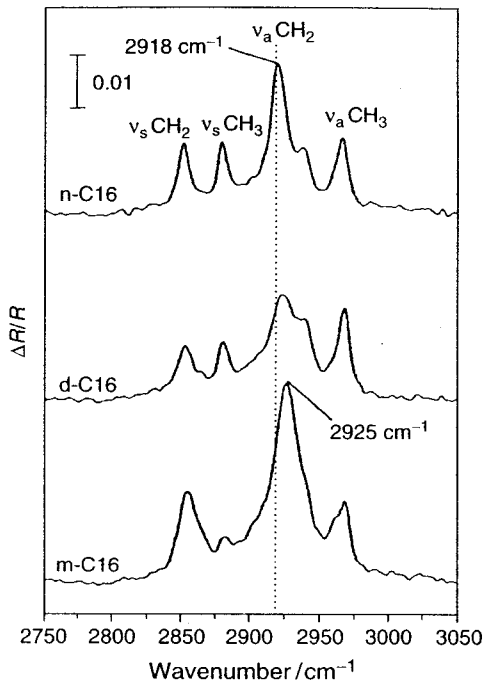

Figure 9. PM-IRRAS spectra of SAMs generated from hexadecanethiol (n-C16), 2,2-ditetradecylpropane-1,3-dithiol (d-C16), and 2-tetradecylpropane-1,3-dithiol (m-C16). (Reproduced from Shon *et al.*[14] with permission from the American Chemical Society.)

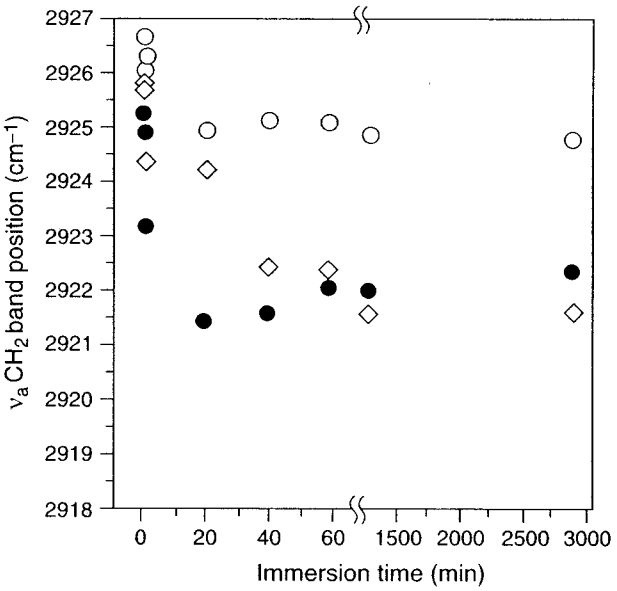

Figure 10. Adsorption profiles as measured by PM-IRRAS of aromatic dithiol **1** (●), aromatic monothiol **2** (◇), and aromatic disulfide **3** (○) in iso-octane. (Reproduced from Shon *et al.*[15] with permission from the American Chemical Society.)

function of immersion time for three types of compounds. Notice that compounds **1** and **2** both level off at about 2922 cm^{-1}, but that **1** requires only 20 min to achieve its well-ordered monolayer, whereas **2** takes roughly twice as

long. The difference in rate of adsorption was attributed to the fact that **1** has two thiol functional groups per molecule and **2** only has one. These data were compiled from ex situ PM-IRRAS spectra; in other words, the gold samples were allowed to sit in the appropriate solution for a certain immersion time, then they were removed, rinsed, and blown dry with nitrogen. These ex situ spectra yield useful information, but do not take full advantage of the power of PM-IRRAS. In subsequent sections, we will see in situ measurements of alkanethiol monolayers. Furthermore, the examples thus far have only shown the CH region of PM-IRRAS spectra, which is necessarily less difficult than the fingerprint region since there are no atmospheric interferences.

3.1.2 SAMs in the fingerprint region

PM-IRRAS has been used to characterize SAMs in the fingerprint region while completely eliminating vapor-phase water absorptions from the spectra. As seen above, alkanethiols on gold form very nice monolayers. These SAMs can serve as a starting point for further chemistry by reactions with terminal functional groups as shown in Figure 11.[16] By activating the terminal carboxylic acid group with 1-ethyl-3-[3-(dimethylamino)propyl] carbodiimide (EDC) and *N*-hydroxysulfosuccinimide (NHSS), the monolayer molecules will react with amines. The simplest case used ammonia and resulted in the conversion of the acid to the amide. This chemistry was followed with PM-IRRAS as seen in Figure 12. Initially, in Figure 12(a), the dominant peaks are due to carboxylic acid and carboxylate stretches at 1740 cm^{-1} and 1400 cm^{-1}, respectively. Figure 12(b), (c) and (d) show the results after each of three successive reaction cycles (EDC/NHSS followed by NH_3). The three most prominent peaks now occur at 1675 cm^{-1}, 1610 cm^{-1}, and 1408 cm^{-1}, which relate to the carbonyl stretching, N–H bending, and C–N stretching vibrations of the amide functional group. The remaining shoulder in Figure 12(d) at 1715 cm^{-1} indicates that some of the carboxylic acid groups (ca. 20%) were not converted to the amide.

Further evidence of the chemistry occurring was obtained from spectra of the intermediate NHSS ester monolayer for each reaction cycle (see Figure 13). These spectra show many sharp peaks, the most important of which is the strong band at 1820 cm^{-1}. This band is the stretching vibration of the MUA carbonyl in the form of an NHSS ester, which proves that a reaction has occurred on the surface because this band is not present in the spectrum of either MUA or NHSS itself. Notice that this 1820 cm^{-1} band decreases in intensity during each successive reaction cycle as fewer MUA molecules are available due to prior conversion to

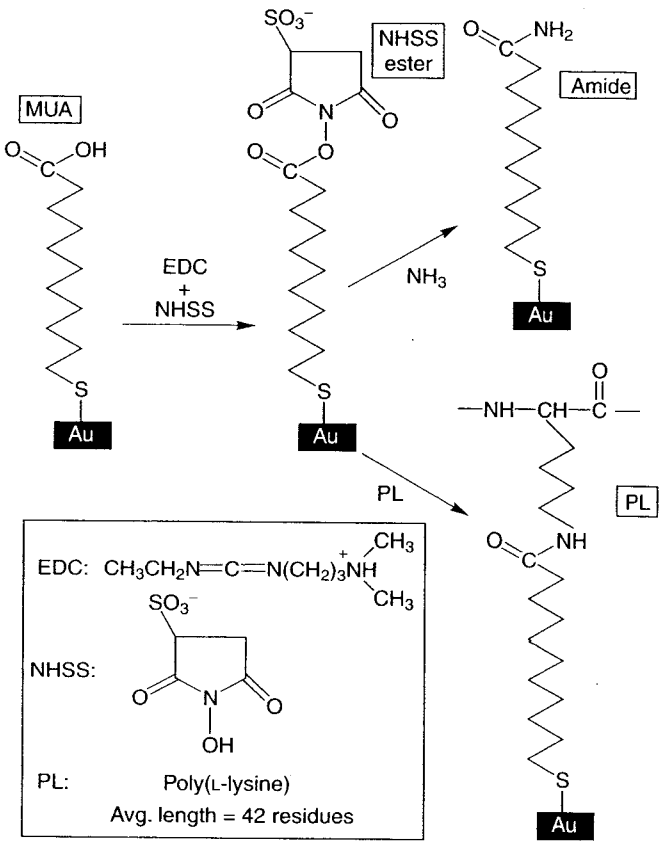

Figure 11. Reaction scheme for forming amide bonds with a SAM of 11-mercaptoundecanoic acid (MUA) on a gold surface. In the first step, the MUA carboxylic acid groups are reacted with the carbodiimide, EDC, and then NHSS to form the NHSS ester. Subsequent reaction of this actived intermediate with an aqueous solution of either ammonia (NH_3) or pLys results in the attachment of these amines to the surface by formation of an amide bond. (Reproduced from Frey and Corn[16] with permission from the American Chemical Society.)

amides. Although the spectrum is not shown, a fourth reaction cycle yielded no detectable band at 1820 cm^{-1} thereby affirming that all of the accessible carboxylic acids had been converted to amides.

PM-IRRAS has been able to follow these monolayer reactions quite easily. Notice the vertical scale in Figure 12. Bands as small as 1×10^{-4} absorbance units, such as the methylene scissors deformation at 1468 cm^{-1}, are easily observed above the peak-to-peak noise of 5×10^{-5}. This low noise was achieved with only 1000 sample scans (I_{diff}) and only 200 background scans (I_{avg}). With the normal mirror velocity of 40 kHz and a resolution of 2 cm^{-1}, these absorbance spectra were obtained in less than 20 min. Furthermore, as promised, these ex situ spectra show absolutely no water vapor absorptions. Purging with dry air was performed, but it was not rigorous purging – the scan was started within a couple minutes after putting the sample into the purge box of the instrument. Purging is not required

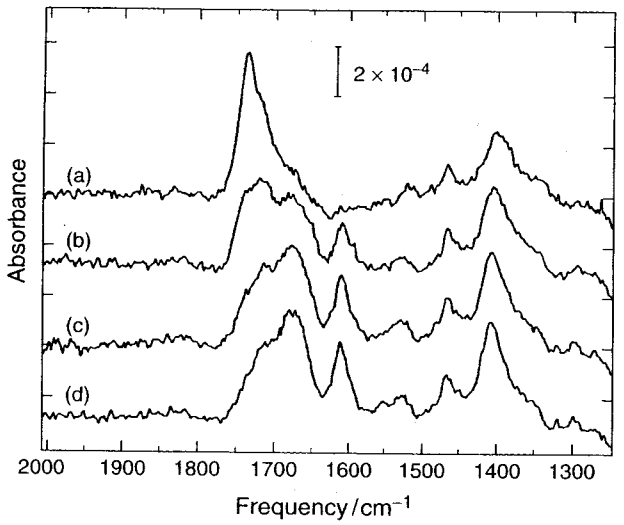

Figure 12. PM-IRRAS spectra showing the gradual conversion of a MUA SAM to an amide monolayer. (a) A MUA SAM with the characteristic carboxylic acid (COOH) band at 1740 cm^{-1}. (b) After reaction of the MUA with EDC/NHSS and then NH_3, partial conversion to the amide is observed. (c) A second cycle of EDC/NHSS and NH_3 converts even more COOH to amides. (d) After the third reaction cycle, nearly complete conversion to the amide is achieved, as indicated by the loss of the COOH band along with increases in the amide bands. (Reproduced from Frey and Corn[16] with permission from the American Chemical Society.)

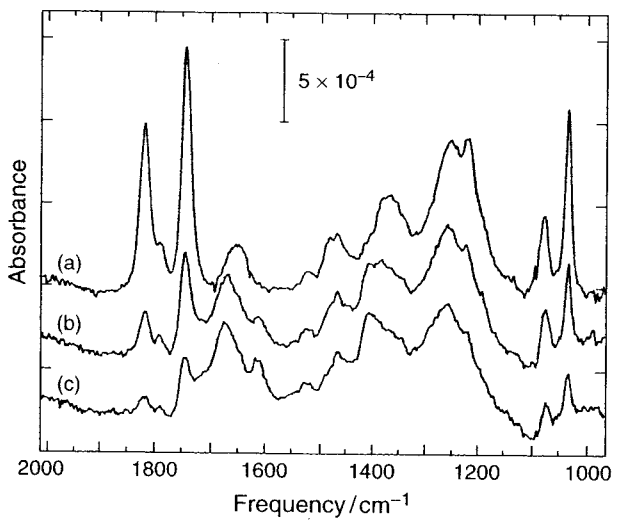

Figure 13. PM-IRRAS spectra of the intermediate NHSS ester layers for the same sample used in Figure 12. (a) NHSS ester monolayer obtained in the first reaction cycle of the MUA SAM with EDC/NHSS. (b) NHSS ester layer from the second cycle. (c) NHSS ester layer from the third cycle. The 1820 cm^{-1} band signifies the formation of MUA-NHSS esters as opposed to merely adsorption of NHSS onto the surface. (Reproduced from Frey and Corn[16] with permission from the American Chemical Society.)

for PM-IRRAS, but it usually offers slight improvements in spectra. One reason is that the water vapor absorbs a significant amount of the infrared light, and the lower incident energy decreases the S/N. Another reason for purging is to prevent significant changes in water vapor concentration between the sample (I_{diff}) and background (I_{avg}) scans. In the example above, block averaging was performed with each block of scans requiring about 1 min. A second ADC (dual-channel mode) would make vapor-phase changes irrelevant, but would not prevent the loss of incident energy. Nonetheless, PM-IRRAS will still provide nice spectra without a dry air purge. Further examples of PM-IRRAS eliminating signals due to bulk-phase species are presented in the following in situ sections.

3.2 Metal surfaces – liquid phase in situ

3.2.1 Structural studies of SAMs

As a first example of the in situ capabilities of PM-IRRAS, we have chosen to continue the story of alkanethiol monolayers on gold. Anderson and co-workers used PM-IRRAS to evaluate the structure of various length alkanethiol monolayers when in contact with D_2O or CD_3CN.[17] Figure 14 shows ex situ and in situ spectra for three different chain length alkanethiol monolayers, namely octadecanethiol (C18), tetradecanethiol (C14), and decanethiol (C10). The spectral changes occurring upon immersion in

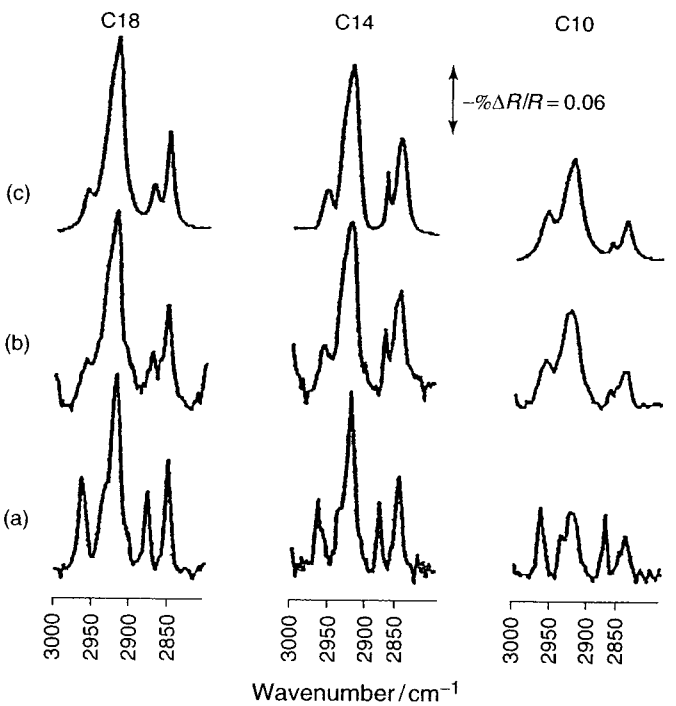

Figure 14. PM-IRRAS spectra of monolayers prepared from octadecanethiol (C18), tetradecanethiol (C14), and decanethiol (C10) in the presence of (a) air and (b) D_2O. (c) Representative composite curve fit spectra of the in situ data. (Reproduced from Anderson *et al.*[17] with permission from the American Chemical Society.)

D_2O are similar regardless of alkanethiol chain length. The methylene bands (peaks near 2920 cm^{-1} and 2850 cm^{-1}) broaden and shift to higher energy by a couple of wavenumbers, indicative of a minor disordering of the monolayer. The most dramatic change, however, is the large decrease in intensity of the methyl bands (peaks near 2965 cm^{-1} and 2880 cm^{-1}). Recall the IRRAS selection rule that requires a component of the vibrational mode perpendicular to the metal surface. Thus, the diminished intensity of these bands can be attributed to a change in orientation of the methyl group. The authors conclude from these results that the structural changes occur primarily in the outer portions of the monolayer in order to minimize penetration of water into the monolayer. Interestingly, when the C10 monolayer is immersed into an organic solvent, CD_3CN, the methyl bands dramatically *increase* in intensity (spectra not shown). This opposite effect from the D_2O results can be explained by a change in methyl group orientation so as to allow solvent penetration in this case.

3.2.2 *Electrochemical studies*

The sensitivity and surface selectivity of PM-IRRAS is demonstrated dramatically in the following example of a time-dependent, in situ examination of an electrochemical reaction occurring on the surface of a thin gold film. The chemical system studied by Cheng and Corn is shown in Figure 15.[18] The first step was to create a hydrophilic thin film by sequential adsorption of oppositely charged polyamino acids, poly(L-lysine) (pLys) and poly(L-glutamic acid) (pGlu). The ex situ PM-IRRAS spectra in Figure 16 nicely show the buildup of the polyelectrolyte multilayer via the amide I and II bands of the polypeptide backbones as well as the carboxylate stretch of the pGlu. The next step led to the incorporation of electroactive ions into these films by immersion in a 1 : 1 solution of ferrocyanide, $Fe(CN)_6^{4-}$, and ferricyanide, $Fe(CN)_6^{3-}$. After 30 min the sample was removed, rinsed with water and dried with nitrogen. The ex situ PM-IRRAS spectra in Figure 17 show a large band at 2040 cm^{-1} assigned to ferrocyanide ions and a much smaller band at 2110 cm^{-1} assigned to ferricyanide. The discrepancy in peak size, along with other experiments, indicated preferential incorporation of the more highly charged ferrocyanide ion.

In order to follow the electrochemical oxidation of ferrocyanide to ferricyanide, in situ PM-IRRAS was performed.[19] An 11-layer pLys/pGlu film with incorporated ferrocyanide ions was immersed into a 1,2-dichloroethane solution containing 10 mM electrolyte. The in situ spectrum of this film is shown as the solid line in Figure 18. Stepping the potential to +0.67 V for 2 min resulted in a 50% decrease in the 2040 cm^{-1} ferrocyanide peak and

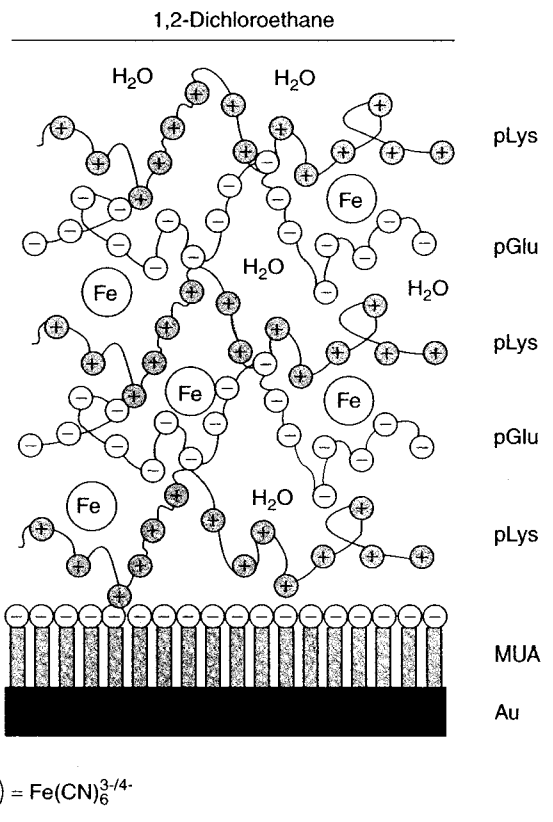

Figure 15. Schematic representation of a thin polypeptide multilayer film assembled on a negatively charged MUA-modified gold surface by the sequential adsorption of positively charged pLys and negatively charged pGlu. Water and ferri/ferrocyanide ions can be incorporated inside the film. Some small counterions are omitted for clarification. A liquid/liquid interface is formed when the multilayer film is immersed in 1,2-dichloroethane. (Reproduced from Cheng and Corn[18] with permission from the American Chemical Society.)

a significant increase in the 2113 cm^{-1} ferricyanide peak, which spectroscopically confirmed the oxidation reaction. Applying the potential for longer times yielded further conversion to the oxidized species.

The time resolution of 2 min for in situ PM-IRRAS is quite extraordinary, and results from several experimental factors. The relatively thick 11-layer film gave large signals, but it is quite clear that thinner films would produce good spectra as well. An InSb detector was used and it is much more sensitive than the more common MCT; its drawback, however, is its cutoff near 1800 cm^{-1}, which precludes its use in the fingerprint region. Another important experimental feature was making the layer of solution (in this case dichloroethane plus electrolyte) as thin as possible by pressing the sample against a CaF_2 prism. The infrared light enters and exits through the prism and only has to traverse a very small span of solution on its way to and from the gold sample. Attention to these details

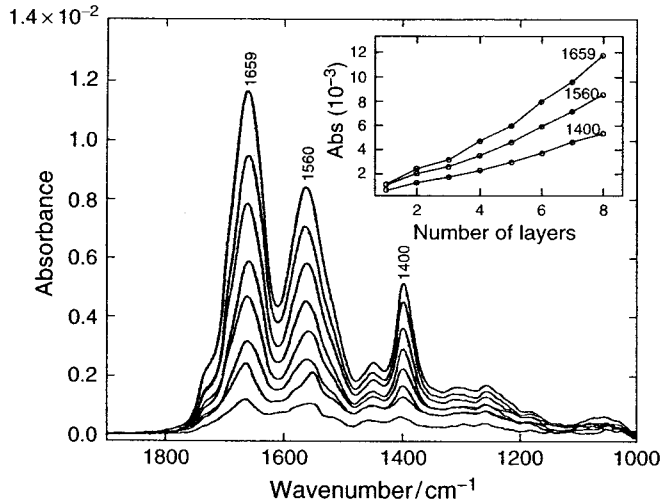

Figure 16. Ex situ PM-IRRAS spectra of pLys/pGlu multilayer films assembled on a MUA-modified gold surface. The concentration of the pLys and pGlu solutions was 2 mg mL^{-1} in 0.1 M phosphate buffer (pH = 8.0), and the assembly time was 30 min. The inset shows the increase in absorbance of the amide I and II bands and the carboxylate symmetric stretch (1400 cm^{-1}) band with the number of layers deposited. (Reproduced from Cheng and Corn[18] with permission from the American Chemical Society.)

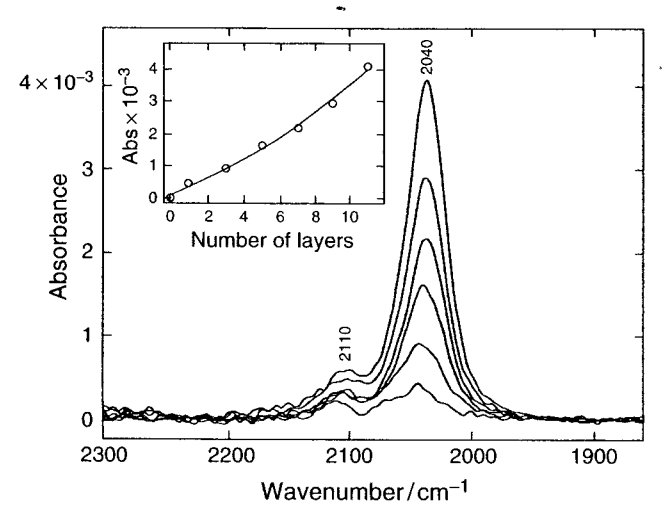

Figure 17. Ex situ PM-IRRAS measurements of ferri/ferrocyanide incorporation into pLys/pGlu multilayer films consisting of 1, 3, 5, 7, 9, and 11 layers. Each film was immersed in a 1.0 mM ferri/ferrocyanide solution (0.1 M phosphate buffer, pH = 5.6) for 30 min, rinsed with water, and dried under a N_2 stream. The inset plots the change in absorbance of the CN stretch band (2040 cm^{-1}) with the number of layers adsorbed on the surface. The ferri/ferrocyanide incorporation was carried out after the corresponding numbers of pLys and pGlu layers were assembled at pH = 8.0. (Reproduced from Cheng and Corn[18] with permission from the American Chemical Society.)

produced excellent liquid-phase in situ spectra in short time periods.

Another example of aqueous in situ PM-IRRAS has been published, in which spectra are shown throughout

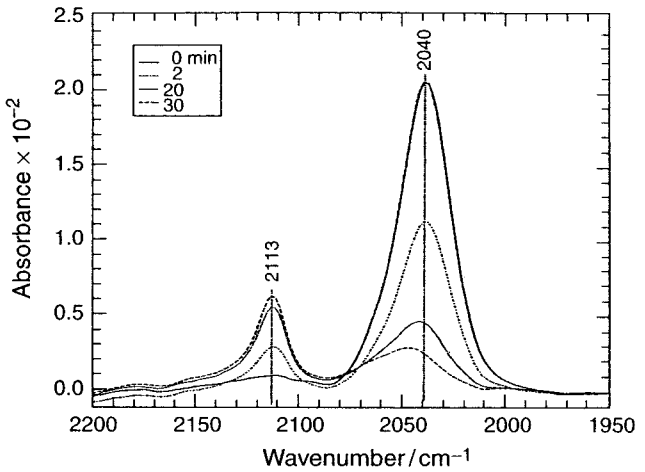

Figure 18. In situ PM-IRRAS spectra of an 11-layer film showing the progress of the oxidation of bound ferrocyanide as a function of time. The applied potential was first held at −0.48 V and then switched to 0.67 V for different periods of time as indicated. (Reproduced from Cheng *et al.*[19] with permission from Elsevier Science.)

the mid-infrared region.[20] Although peaks due to bulk-phase water do still appear, they are much smaller and more reproducible than for conventional IRRAS. Consequently, more information can be obtained from the PM-IRRAS spectra. The next section discusses gas-phase in situ experiments that do not require such a thin bulk-phase layer in order for PM-IRRAS to completely eliminate bulk-phase absorptions from the spectra.

3.3 Metal surfaces – gas phase in situ

3.3.1 Corrosion studies on copper

Even gas-phase in situ studies can be difficult without a completely surface-selective technique. That is why IRRAS without PM has had difficulty probing surface adsorption in the presence of the reactant gases or high humidity levels. In fact, due to the relatively small signal size and the overwhelming contribution from water vapor, not only are the water O–H stretching and H–O–H bending regions obscured, but a large portion of the mid-infrared spectrum (1900–1300 cm^{-1}) is adversely affected by the water vapor bending absorption.[10] As this following example demonstrates, with PM the 1900 to 1300 cm^{-1} spectral region becomes accessible; adsorbed and bound water becomes observable, and there is a net overall improvement in analytical sensitivity.

Faguy *et al.*[10] have performed corrosion studies of a copper surface exposed to various combinations of SO_2, NO_2, and HCl in the presence of high humidity (relative humidity 75%). Figures 19 and 20 compare the PM-IRRAS

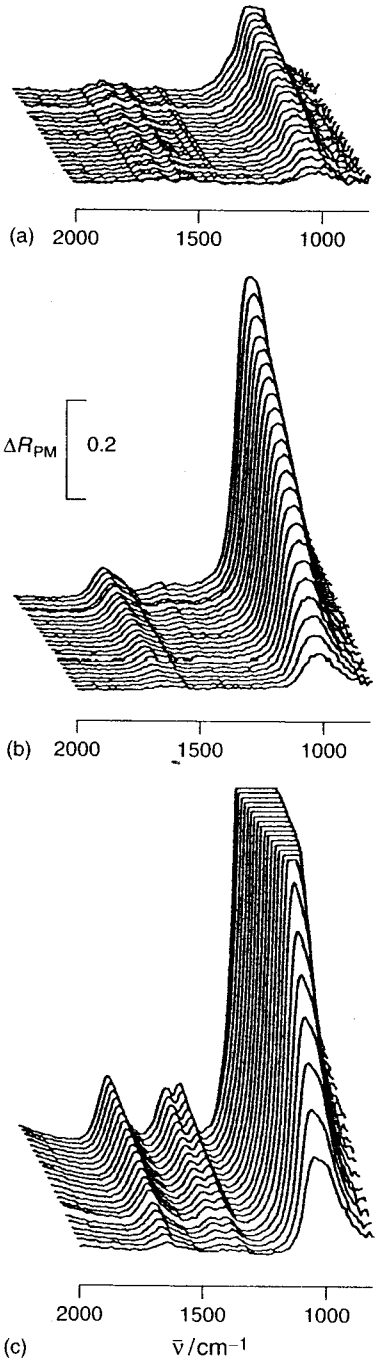

Figure 19. A comparison of ΔR_{PM} time-evolved spectra, 2000 to 800 cm^{-1}, from 15.7 to 136 min upon exposure to: (a) 322 ppbv SO_2, (b) 322 ppbv SO_2, 264 ppbv NO_2, (c) 322 ppbv SO_2, 264 ppbv NO_2, and 13 ppbv HCl. All spectra have the same intensity scale. (Reproduced from Faguy *et al.*[10] with permission from the Society of Applied Spectroscopy.)

data over 136 min of treatment for three different purge-gas compositions. These time-differential spectra were obtained by ratioing each spectrum to an initial spectrum. This data work-up most clearly shows changes as corrosion occurs and removes the broad periodic background. In each figure,

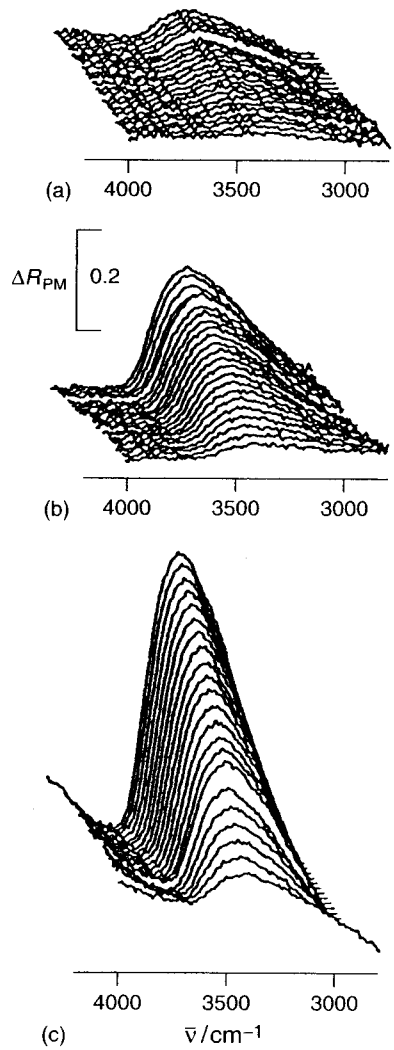

Figure 20. A comparison of ΔR_{PM} time-evolved spectra for the 4200 to 2800 cm^{-1} region under the same experimental conditions as in Figure 19. (Reproduced from Faguy *et al.*[10] with permission from the Society of Applied Spectroscopy.)

the three stack plots clearly show the presence of bound water via the H–O–H bend at 1635 cm^{-1} in Figure 19 and the O–H stretching band at 3400 cm^{-1} in Figure 20. Since these band profiles differ among the three experiments, it may be possible to infer orientation of the bound water. Also evident in Figure 19 are other peaks due to S–O and N–O stretching bands of various surface-bound species. Just as impressive as the observed peaks is the fact that no gaseous water modes can be distinguished from the noise in the mid-infrared region.

It is quite apparent from the three experiments represented in Figure 19 that corrosion rates vary considerably depending upon which gases are present, and in particular HCl greatly increases the rate. The experiments all used approximately the same humidity level but different combinations of corrosive gases: (a) SO_2 alone, (b) SO_2

and NO_2, and (c) SO_2, NO_2, and HCl. When HCl is present in trace amounts, and when SO_2 and NO_2 are in similar sub-ppm concentrations, water is incorporated into a growing corrosion film approximately 2.5 times faster than when no HCl is present in the same moist SO_2- and NO_2-containing air. Considering the physical optics of the grazing-angle reflection experiment, two caveats need to be made. First, it was assumed that the film was thin enough that a linear relationship existed between absorbance and amount of adsorbed water. Second, while the signal is proportional to the amount of bound water at the metal surface, an absolute quantitative determination from the infrared data alone is not possible and would require an additional measurement technique such as surface plasmon resonance (see **Fourier Transform Surface Plasmon Resonance**).

Another conclusion the authors were able to draw from these data was that bound water was the only source of the ν_{OH} signal, as opposed to bound hydroxide. They proved this by correlating the ν_{OH} signal with the δ_{HOH} signal and found strong statistical correlation. If corrosion was allowed to occur for much longer times, >5 h, a sharp band at 3544 cm^{-1} grows in, indicating a surface hydroxide. Not only did PM-IRRAS allow careful observation of surface-bound water species in the presence of gaseous water, but the PM technique provided a S/N increase of 2.5 times over that of IRRAS. For these kinds of spectrometric experiments, the S/N will increase by a factor proportional to the square root of the number of co-added scans. Consequently, another way of expressing the enhancement of 2.5 is by squaring it to show that PM-IRRAS allows a six-fold decrease in equivalent sampling time, which can lead to better time resolution for kinetic studies of corrosion or other chemical processes.

3.3.2 *Carbon monoxide on Co(0001)*

PM-IRRAS was applied to an in situ analysis of a model system of heterogeneous catalysis, namely carbon monoxide adsorption onto a cobalt surface. This system is of great interest in the Fischer–Tropsch reaction converting CO and H_2 into long-chain hydrocarbons. Previous studies of the surface chemistry were done under UHV conditions, despite the fact that the commercial process involves pressures of 5–30 bar. Beitel *et al.*[21] performed PM-IRRAS over a very large range of pressures (10^{-10} mbar up to 600 mbar) in order to tie together UHV studies with those done at high pressure. For example, prior UHV and low-temperature studies had shown that a transition occurs in the adsorbed CO layer as the CO coverage increases. PM-IRRAS results affirmed that this transition also occurs at high pressure and room temperature, thereby providing information about conditions many orders of magnitude closer to those of the Fischer–Tropsch process.

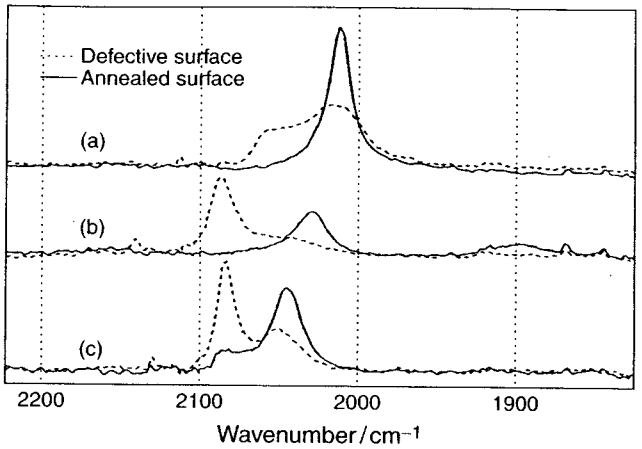

Figure 21. Influence of surface defects on the CO-adsorption layer by comparison of a sputtered (defective) and an annealed (defect-free) surface; PM-IRRAS spectra showing the CO absorption region (a) after 10 langmuirs of CO dosing at room temperature in UHV, (b) at the CO pressure of 100 mbar at room temperature, and (c) at a CO pressure of 100 mbar at 490 K. (Reproduced from Beitel *et al.*[21] with permission from the American Chemical Society.)

In a further investigation, PM-IRRAS easily provided the sensitivity and resolution to distinguish between CO adsorbed to normal surface sites versus those molecules bound to defect sites.[21] Many reactions involving heterogeneous catalysts are believed to occur at defect sites on the surface, which makes investigation of adsorption there of the utmost importance. Figure 21 shows spectra for an annealed, defect-free surface (solid lines) and spectra for a surface with many defects due to argon sputtering (dashed lines). In the dashed-line spectra, the peaks near 2080 cm^{-1} were attributed to CO attached to defect sites. The authors report many interesting findings from these spectra and discuss them with regard to what has been found on other surfaces, but only a couple of those findings will be presented here. The change between spectra (b) and (c) results from an increase in temperature from 300 to 490 K. For the annealed, defect-free surface, heating resulted in the formation of some defect sites as evidenced by the CO adsorbing to those sites and giving a small band at 2080 cm^{-1} (solid line spectrum (c)). Even more interesting is the sharpening of the 2080 cm^{-1} peak in the dashed-line spectrum upon heating the cobalt surface. This sharpening without a concomitant intensity increase was reported to result from surface ordering whereby many point defects aggregated into islands.

3.3.3 *Organic vapors on silicon dioxide nanoparticle thin films on gold*

At Lake Forest College we have set up in situ PM-IRRAS and used it to study adsorption onto a surface under high

concentrations of organic vapors. The corrosion study of copper discussed above used very small concentrations (ppbv) of the reactant gases, which would not produce large bulk-phase absorptions. That work did show, however, the complete removal of gaseous water peaks. Our PM-IRRAS results further emphasize this surface selectivity, while giving information about adsorption occurring onto an important thin film.

The system we chose to study was adsorption of organic vapors onto silicon dioxide nanoparticle thin films on a gold surface. These films were prepared on top of a carboxylic acid terminated alkanethiol monolayer by alternating exposure to polylysine, a polycation, and negatively charged silicon dioxide nanoparticles. Once the film was formed, PM-IRRAS spectra were recorded in an in situ cell purged with nitrogen and subsequently purged with approximately 10% acetone vapor in nitrogen. Since the adsorption of acetone is a completely reversible process, all measurements have to be made in situ, which makes PM-IRRAS a great choice.

Figure 22 shows a differential spectrum between the thin film during acetone dosing and the thin film under nitrogen. Large positive-going acetone bands are observed at 1706, 1424, and 1368 cm^{-1}. A control experiment performed on a surface without the nanoparticle film yielded a totally flat differential spectrum. Consequently, these experiments prove not only that acetone adsorbs to the nanoparticle film, but also that PM-IRRAS has completely eliminated vapor-phase absorptions from a very concentrated organic vapor.

The other peaks in Figure 22 relate to changes in adsorbed water and changes occurring with the SiO_2 nanoparticles upon adsorption of acetone. The large negative-going peak at 1225 cm^{-1} (cut off in the figure), the negative-going 1269 cm^{-1} peak, and the positive-going 1145 cm^{-1} peak all result from changes in Si–O stretching bands. The final feature to explain is the broad negative-going band at 1635 cm^{-1}, which is attributed to loss of adsorbed water molecules. Further PM-IRRAS experiments will explore preferential adsorption occurring under simultaneous exposure to multiple vapors.

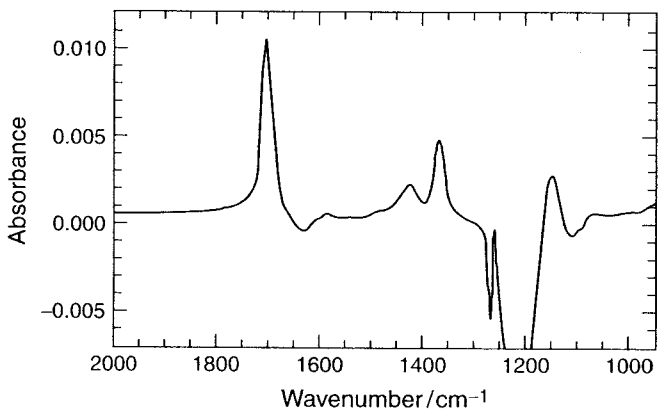

Figure 22. In situ PM-IRRAS differential spectrum showing adsorption of acetone vapor onto a thin film containing SiO_2 nanoparticles.

3.4 Air/water interface

PM-IRRAS experiments at the air/water interface differ somewhat from those at metal surfaces both in terms of the setup and the resulting spectra (see **Infrared Reflection–Absorption Spectrometry of Monolayer Films at the Air–Water Interface**). The optical layout and signal processing is quite similar to that for metal surfaces with the primary difference being an extra pair of mirrors to reflect the light onto and collect the light from the horizontal water surface. A chief consideration is the best angle of incidence for PM-IRRAS. Dluhy[22] gave an extensive report of the reflectance, phase shift, and electric field intensity as a function of incident angle. He concluded that low incident angles (0°–40°) are optimal for IRRAS studies at the air/water interface. However, the addition of PM places greater importance on having a large difference between the two polarizations. Consequently, the best angle of incidence becomes 76° from the surface normal (Figure 23).[23] The node at 57° indicates that no absorptions would be observed for this incident angle. On either side of this node are local maxima at 38° and 76°. These maxima have approximately equal magnitude, but experimentally Turlet and co-workers found that 76° gave much better S/N and made it worth the extra difficulty of using an angle nearer to the grazing incidence.

PM spectra from the air/water interface have a few interesting differences from those at metal surfaces. At an

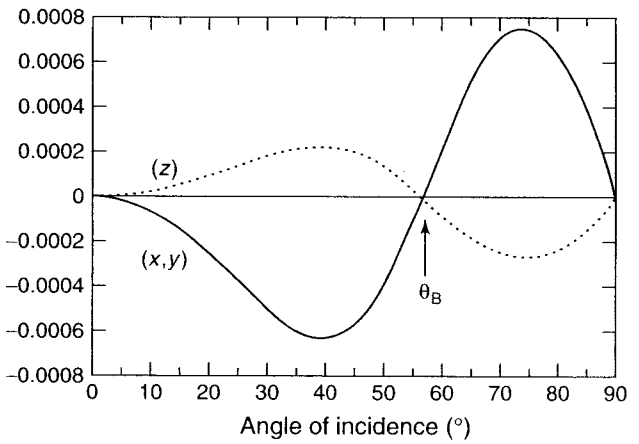

Figure 23. Behavior vs the angle of incidence of the theoretical PM-IRRAS difference signal from a uniaxial spread monolayer having an absorption band with its transition moment oriented along the surface (solid line) or perpendicular to the surface (dashed line). (Reproduced from Blaudez *et al.*[23] with permission from the Society of Applied Spectroscopy.)

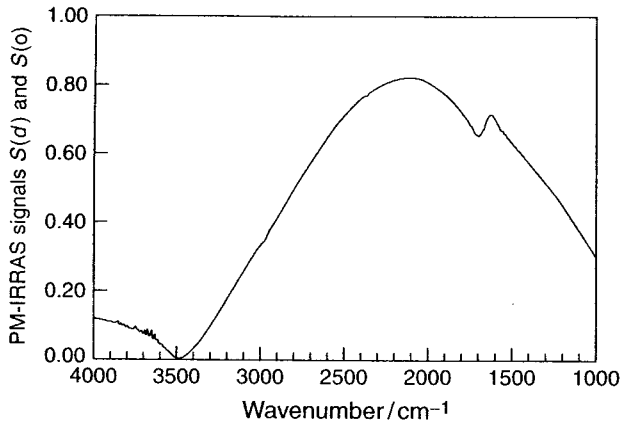

Figure 24. PM-IRRAS spectrum from a monolayer of deuterated arachidic acid spread on the water surface and PM-IRRAS spectrum from the uncovered water interface. These two spectra have been recorded with exactly the same experimental settings and, as can be seen, superimpose almost perfectly. (Reproduced from Blaudez *et al.*[23] with permission from the Society of Applied Spectroscopy.)

angle of incidence of 76°, surface selection rules show that vibrations with transition moments in the plane of the interface yield positive-going peaks, whereas those normal to the interface yield negative-going peaks.[24] Interestingly, if the incident angle were 38°, these directions would be switched. Transition moments poised at 52° from the plane of the air/water interface yield no spectral features whatsoever. These selection rules may be used to determine the orientation of molecules at the interface as shown in the example below. One more feature of every PM-IRRAS spectrum from the air/water interface is a broad dispersion-like peak near 1650 cm^{-1} (Figure 24). This feature is due to the δ_{HOH} bending mode of water molecules from the subphase, but fortunately its intensity is constant. Consequently, spectra are usually shown as a ratio between the monolayer-covered surface and the uncovered water surface.

Desbat and co-workers at the Université de Bordeaux I in France have applied PM-IRRAS at the air/water interface to numerous problems. A recent interesting example involved finding the anisotropic optical constants, in the mid-infrared, of bacteriorhodopsin (bR) with subsequent determination of the average tilt angle of its α helices.[25] The PM-IRRAS spectrum of a bR monolayer in Figure 25 shows a broad dispersion-like shape for the amide I band (1740 to 1600 cm^{-1}) as well as a positive-going amide II band at 1540 cm^{-1}. The dashed line in the figure corresponds to a calculated spectrum using the optical constants and the tilt angle of 27° determined for a bR monolayer on a *solid* substrate. The lack of agreement led them to try different optical constants and tilt angles until they obtained the calculated spectrum shown in Figure 26.

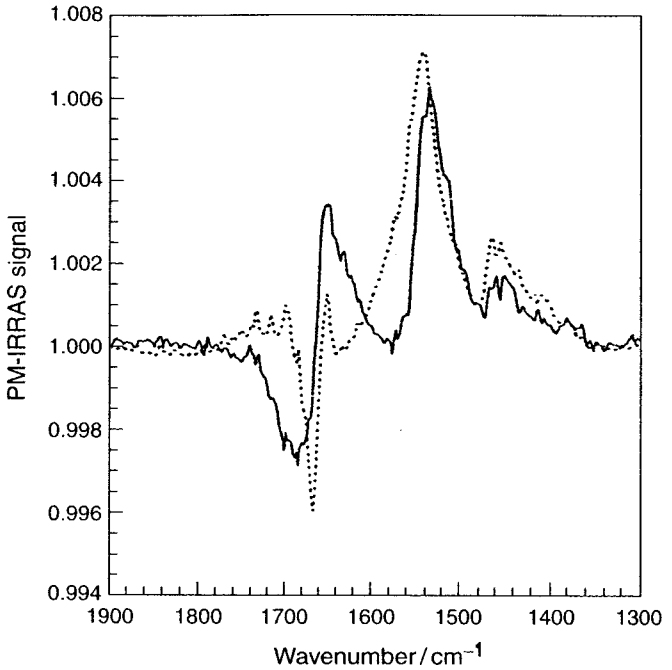

Figure 25. Experimental (solid line) and calculated (dashed line) PM-IRRAS spectra of one bR monolayer spread at the air/water interface. (Reproduced from Blaudez *et al.*[25] with permission from the Society of Applied Spectroscopy.)

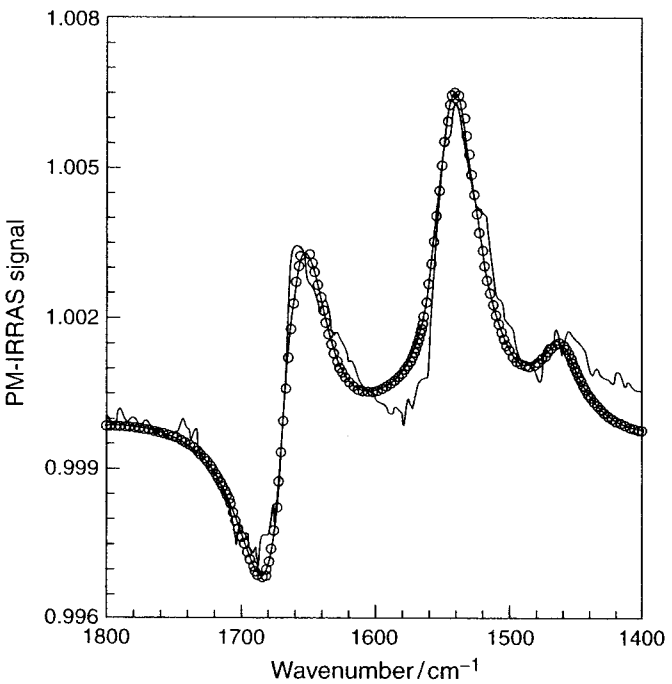

Figure 26. Experimental (solid line) and calculated (circles) PM-IRRAS spectra of one bR monolayer spread at the air/water interface. Calculation was made using modified optical constants of bR. (Reproduced from Blaudez *et al.*[25] with permission from the Society of Applied Spectroscopy.)

The excellent agreement with the experimental spectrum indicates that the tilt angle is 36° at the air/water interface for the α helices of bR. Their findings have major implications in the area of transferring bR or other monolayers or bilayers from the air/water interface onto solid surfaces.

4 SUMMARY

A PM approach to IRRAS has numerous advantages over conventional IRRAS. One of the most important considerations is that PM-IRRAS obviates the need for a separate background spectrum of a "clean" substrate, which is frequently difficult to prepare. With PM-IRRAS, both the "background," $(I_p + I_s)$, and "sample" $(I_p - I_s)$, interferograms are obtained almost simultaneously from the same sample surface. Thus, not only is a reference surface not needed, but also baseline fluctuations caused by instrument drift are prevented. In addition to this advantage, many PM-IRRAS measurements have benefited from the elimination of atmospheric signals and an improved S/N. In situ experiments have taken full advantage of PM's surface selectivity. With liquid-phase in situ PM-IRRAS, bulk-phase absorptions are still observed, but are much smaller than with conventional IRRAS. For gas-phase in situ experiments, however, PM-IRRAS completely eliminates absorption bands of the bulk phase from the spectrum, as seen in several examples discussed in this article. By overcoming many of the experimental challenges of reflection–absorption spectroscopy, the PM approach has developed into a beneficial and widely used technique for vibrational spectroscopy of surfaces.

ABBREVIATIONS AND ACRONYMS

ADC	Analog-to-digital Converter
bR	Bacteriorhodopsin
EDC	1-Ethyl-3-[3-(dimethylamino)propyl] Carbodiimide
EFL	Effective Focal Length
MUA	11-Mercaptoundecanoic Acid
NHSS	*N*-Hydroxysulfosuccinimide
pGlu	Poly(L-glutamic acid)
pLys	Poly(L-lysine)
PM	Polarization Modulation
SAM	Self-assembled Monolayer
SSD	Synchronous Sampling Demodulator
UHV	Ultrahigh Vacuum

REFERENCES

1. P.R. Griffiths and J.A. de Haseth, 'Fourier Transform Infrared Spectrometry', John Wiley & Sons, New York (1986).
2. A.E. Dowrey and C. Marcott, *Appl. Spectrosc.*, **36**(4), 414 (1982).
3. R.G. Greenler, *J. Chem. Phys.*, **44**(1), 310 (1966).
4. V.G. Gregoriou, R. Hapanowicz, S.L. Clark and P.T. Hammond, *Appl. Spectrosc.*, **51**(4), 470 (1997).
5. J.D. Swalen and J.F. Rabolt, 'Characterization of Orientation and Lateral Order in Thin Films by Fourier Transform Infrared Spectroscopy', in "Fourier Transform Infrared Spectroscopy", eds J.R. Ferraro and L.J. Basile, Academic Press, New York, Volume 4, Chapter 7 (1985).
6. W.G. Golden, 'Fourier Transform Infrared Reflection–Absorption Spectroscopy', in "Fourier Transform Infrared Spectroscopy", eds J.R Ferraro and L.J. Basile, Academic Press, New York, Volume 4, Chapter 8 (1985).
7. G.C. Chen, P.L. Polavarapu and S. Weibel, *Appl. Spectrosc.*, **48**(10), 1218 (1994).
8. B. Wang, *Spectroscopy*, **12**(1), 30 (1997).
9. B.J. Barner, M.J. Green, E.I. Saez and R.M. Corn, *Anal. Chem.*, **63**, 55 (1991).
10. P.W. Faguy, W.N. Richmond, R.S. Jackson, S.C. Weibel, G. Ball and J.H. Payer, *Appl. Spectrosc.*, **52**(4), 557 (1998).
11. M.J. Green, B.J. Barner and R.M. Corn, *Rev. Sci. Instrum.*, **62**(6), 1426 (1991).
12. K.W. Hipps and G.A. Crosby, *J. Phys. Chem.*, **83**(5), 555 (1979).
13. T. Buffeteau, B. Desbat and J.M. Turlet, 'Nicolet FT-IR Spectral Lines', Nicolet Instrument Corporation, Madison, WI (1990).
14. Y.S. Shon, R. Colorado, Jr, C.T. Williams, C.D. Bain and T.R. Lee, *Langmuir*, **16**, 541 (2000).
15. Y.S. Shon, R. Colorado, Jr, C.T. Williams, C.D. Bain, N. Garg, J.M. Friedman and T.R. Lee, *Langmuir*, **16**, 4266 (2000).
16. B.L. Frey and R.M. Corn, *Anal. Chem.*, **68**, 3187 (1996).
17. M.R. Anderson, M.N. Evaniak and M. Zhang, *Langmuir*, **12**, 2327 (1996).
18. Y. Cheng and R.M. Corn, *J. Phys. Chem. B*, **103**, 8726 (1999).
19. Y. Cheng, L. Murtomaki and R.M. Corn, *J. Electroanal. Chem.*, **483**, 88 (2000).
20. W.N. Richmond, P.W. Faguy, R.S. Jackson and S.C. Weibel, *Anal. Chem.*, **68**, 621 (1996).
21. G.A. Beitel, A. Laskov, H. Oosterbeek and E.W. Kuipers, *J. Phys. Chem.*, **100**, 12 494 (1996).
22. R.A. Dluhy, *J. Phys. Chem.*, **90**, 1373 (1986).
23. D. Blaudez, T. Buffeteau, J.C. Cornut, B. Desbat, N. Escafre, M. Pezolet and J.M. Turlet, *Appl. Spectrosc.*, **47**, 869 (1993).
24. S. Payan and B. Desbat, *Langmuir*, **12**, 6627 (1996).
25. D. Blaudez, F. Boucher, T. Buffeteau, B. Desbat, M. Grandbois and C. Salesse, *Appl. Spectrosc.*, **53**, 1299 (1999).